materials

MDPI

Article

Structural Design Method for Constructions: Simulation, Manufacturing and Experiment

Pavel Bolshakov [1], Nikita Kharin [2,3], Ramil Kashapov [3] and Oskar Sachenkov [1,2,*]

[1] Department Machines Science and Engineering Graphics, Tupolev Kazan National Research Technical University, 420111 Kazan, Russia; bolshakov-pavel@inbox.ru
[2] Institute of Mathematics and Mechanics, Kazan Federal University, 420008 Kazan, Russia; nik1314@mail.ru
[3] Institute of Engineering, Kazan Federal University, 420008 Kazan, Russia; kashramil.88@mail.ru
* Correspondence: 4works@bk.ru

Abstract: The development of additive manufacturing technology leads to new concepts for design implants and prostheses. The necessity of such approaches is fueled by patient-oriented medicine. Such a concept involves a new way of understanding material and includes complex structural geometry, lattice constructions, and metamaterials. This leads to new design concepts. In the article, the structural design method is presented. The general approach is based on the separation of the micro- and macro-mechanical parameters. For this purpose, the investigated region as a complex of the basic cells was considered. Each basic cell can be described by a parameters vector. An initializing vector was introduced to control the changes in the parameters vector. Changing the parameters vector according to the stress-strain state and the initializing vector leads to changes in the basic cells and consequently to changes in the microarchitecture. A medium with a spheroidal pore was considered as a basic cell. Porosity and ellipticity were used for the parameters vector. The initializing vector was initialized and depended on maximum von Mises stress. A sample was designed according to the proposed method. Then, solid and structurally designed samples were produced by additive manufacturing technology. The samples were scanned by computer tomography and then tested by structural loads. The results and analyses were presented.

Keywords: structural design; porous constructions; additive manufacturing; CT

Citation: Bolshakov, P.; Kharin, N.; Kashapov, R.; Sachenkov, O. Structural Design Method for Constructions: Simulation, Manufacturing and Experiment. *Materials* **2021**, *14*, 6064. https://doi.org/10.3390/ma14206064

Academic Editor: Aleksander Muc

Received: 25 August 2021
Accepted: 12 October 2021
Published: 14 October 2021

1. Introduction

The modern approach for design implants and prostheses implies patient-oriented solutions. Such an approach involves not only new manufacturing methods but also a new vision of the product. Additive manufacturing allows production constructions with complex geometry. However, the solution for the automation of the design of such products is still open. So, nowadays lattice constructions have become popular for this purpose. Yet, the dependence between the different geometries of the lattice, the mechanical properties, and the biological adaptive is being researched [1–3]. Additionally, a manifestation of the brittle properties and the geometry deviations after manufacturing is still an issue of the day [4–7]. By changing the materials and melting modes [8–10], the mechanical parameters can be improved or vice versa. Despite the aforementioned difficulties, it is obvious that additive manufacturing and patient-oriented design can notably increase the quality of the medical treatments.

This article is focused on an approach for the structural design method. Previously, a method for designing a lattice endoprosthesis for long bones was developed [11]. The endoprosthesis was manufactured and passed clinical experiments. The developed approach was generalized. The main idea is based on the bone adaptation analogy. It is known that adaptation can be formulated by Wolff's law [12]. To describe bone tissue orthotropy, a fabric tensor is used. The fabric tensor is also used to calculate the stiffness tensor [12,13]. The foundation of the adaptation model is an alignment of the stress and stiffness tensors.

In terms of the fabric tensor, it means that the orthotropic directions are equal to the stress principal directions [13,14]. The widespread approach is to use representative volumes to determine the fabric tensor and the effective mechanical properties [15,16].

It has been shown [17–19] that implants interact with bone tissue and that the structure and the microstructure of the implant influence the quality of this interaction. Additive manufacturing allows the generation of solid irregular or lattice geometry [20,21], but on the other hand, local microporosity decreases fatigue resistance. Classical post-processing, such as tempering, allows the counteraction of the negative sides of the technology [22,23]. Despite the aforementioned technological barriers, the opening opportunities are promising. The ability to design material within a product opens up new possibilities in patient-specific prostheses [24,25]. The complexity of such an approach appears in defining the external loads and the formulation criteria of the design [26,27]. A novel approach is the use of additive manufacturing technology for liquid crystal elastomers, the exceptional properties of which show good usage in a range of applications in the fields of biology and medicine [28–30].

In this article, a method of structural design is presented. An example of structurally designed construction is presented. The designed and regular constructions were manufactured and compared in natural experiments.

2. Materials and Methods

2.1. Problem Formulation

The mechanical behavior of the region V in R^3 with the boundary ∂V, within the linear theory of elasticity, can be described by the following system of equations [11]:

$$\nabla \cdot \tilde{\sigma} = 0, \ \forall \vec{x} \in V^0 \tag{1}$$

$$\tilde{\varepsilon} = \frac{1}{2}\left(\nabla \vec{u} + \left(\nabla \vec{u}\right)^T\right), \ \forall \vec{x} \in V^0 \tag{2}$$

$$\tilde{\sigma} = \tilde{C} : \tilde{\varepsilon}, \ \forall \vec{x} \in V^0 \tag{3}$$

$$\vec{u} = 0, \ \forall \vec{x} \in S_{kin} \tag{4}$$

$$\tilde{\sigma} \cdot \vec{n} = \vec{p}, \ \forall \vec{x} \in S_{sta} \tag{5}$$

$$S_{sta} \cup S_{kin} = \partial V \tag{6}$$

where $V^\circ = V \cup \partial V$; u is the displacement vector; σ is the stress tensor; ε is the elastic strain tensor; and C is the stiffness tensor. S_{sta} is the surface on which static boundary conditions are specified, and S_{kin} is the surface on which kinematic boundary conditions are specified (see Figure 1).

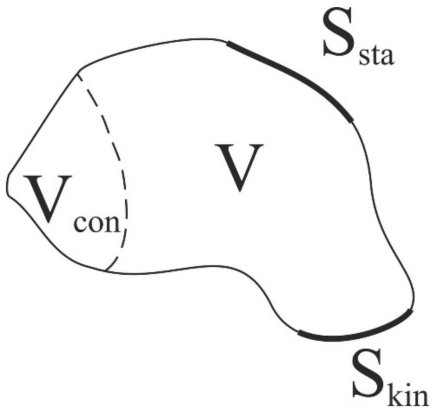

Figure 1. Scheme for problem formulation.

It is necessary to find a distribution of the stiffness tensor C in the volume V such that the stress invariant (in our case, the von Mises stress) reaches a minimum at the constant boundary conditions.

$$\tilde{C} = \tilde{C}(\vec{x}), \max_{\vec{x} \in V'} \|\tilde{\sigma}\| \to \min \tag{7}$$

Applying the design conditions, it is necessary to determine the region V_{con}, in which the components of the tensor of elastic properties remain unchanged:

$$V_{con} \in V^0 \tag{8}$$

Let us call the region V_{con} the constant region. So, V' in (7) can be determined as $V^\circ \backslash V_{con}$. Adding Equation (7) to Equations (1)–(6) allows the formulating of the optimization problem for the structure.

2.2. Structural Problem Formulation

The general idea of the method is that the stress-strain state depends on some of the parameters vectors. Assuming that the anisotropy of the material is provided by the microarchitecture, we consider the forming material isotropic [13,16]. The parameters vector λ describes the material microarchitecture and influences the macro-stiffness tensor. On the other side, we should add an additional vector with initializing parameters, which describe the stress-strain state of the microarchitecture. Let us call it the initializing vector γ, which, obviously, depends on the invariants of the stress tensor f. The initializing vector can be interpreted as the control function of the microarchitecture changes. So, we propose that the stiffness tensor can be presented as a function of the parameters vector, the initializing vector, and the spatial coordinate:

$$\tilde{C} = \tilde{C}\left(\vec{\lambda}\left(\gamma, \vec{x}\right), \vec{\gamma}\left(f(\tilde{\sigma}), \vec{x}\right), \vec{x}\right) \tag{9}$$

Let us consider region V as the number of basic cells. For each basic cell we assume:

$$\begin{cases} \vec{\lambda}\left(\gamma, \vec{x}\right) = \vec{\lambda}(\gamma) \\ \vec{\gamma}\left(f(\tilde{\sigma}), \vec{x}\right) = \vec{\gamma}(f(\tilde{\sigma})) \end{cases} \tag{10}$$

This approach considers a basic cell as a micro-construction with constant macro-properties. The parameters vector λ should be changed according to values of the initializing vector γ. So, if we introduce the control function U the problem can be rewritten:

$$\begin{cases} \vec{\lambda}\left(\gamma, \vec{x}\right) = \vec{\lambda}\left(\gamma, U\left(\vec{x}\right)\right) \\ U\left(\vec{x}\right) = f\left(\vec{\gamma}\left(f(\tilde{\sigma}), \vec{x}\right)\right) \\ \tilde{C} = \tilde{C}\left(\vec{\lambda}\left(\gamma, U\left(\vec{x}\right)\right), \vec{x}\right) \end{cases} \tag{11}$$

This means that the state of the initializing vector γ determines the changes of microarchitecture in terms of the parameters vector λ, and the microarchitecture influences the macro-stiffness tensor. Let us consider the investigated region as a composition of basic cells; each one describes the microarchitecture of a material. Each basic cell can be described by the parameters vectors and can be changed according to the initializing vector. To implement such an approach, the basic cell should be determined in order to define the parameters vector and its relationship with the stiffness tensor.

2.3. Basic Cell

In the research unit, a cube with a spheroidal pore was used as a basic cell. In this case, the parameters vector consists of porosity (λ) and the ellipticity coefficient (β). To investigate the dependence between the stiffness tensor and the parameters vector, a representative elements method was used [31–33]. For this purpose, the parameterized finite element model of a cube with a spheroidal pore was implemented. Twenty-node hexahedral finite elements were used. Kinematic loading was used in the numerical simulation. Uniaxial and shear loads in three directions were implemented. To clarify the mechanical properties, additionally combined (uniaxial with shear) loads were implemented [16,26,34,35]. The parameters were investigated in the interval (0; 1). According to the received data, the functions describing the influence of the parameters on the mechanical properties were found:

$$\begin{cases} \vec{\lambda} = \vec{\lambda}(\lambda, \beta) \\ E_{ii} = E_{ii}\left(\vec{\lambda}\right) \equiv C_{iiii}\left(\vec{\lambda}\right) \\ G_{ij} = G_{ij}\left(\vec{\lambda}\right) \equiv C_{ijij}\left(\vec{\lambda}\right) \\ \nu_{ij} = \nu_{ij}\left(\vec{\lambda}\right) \equiv C_{iijj}\left(\vec{\lambda}\right) \end{cases} \tag{12}$$

For approximation, a fourth-degree polynomial function was used with an approximation error threshold of about 0.9 [33–36]. In the calculations, some of the coefficients were equal to zero, so a common form of the final calculated polynomial was as follows:

$$C_{ijkl}(\lambda, \beta) = c_{00} + c_{10}\lambda + c_{01}\beta + c_{11}\lambda\beta + c_{21}\lambda^2\beta + c_{31}\lambda^3\beta + c_{12}\lambda\beta^2 + c_{22}\lambda^2\beta^2 + c_{13}\lambda\beta^3 \tag{13}$$

where λ and β are components of the parameters vector—porosity and ellipticity, respectively, c_{ij} are coefficients of the polynomial, where i shows the power of porosity and j shows the power of ellipticity. The received values of the coefficients for the approximation polynomial are listed in Table 1.

Table 1. The values of coefficients of approximation polynomial for stiffness parameters.

	c_{00}	c_{10}	c_{01}	c_{11}	c_{21}	c_{31}	c_{12}	c_{22}	c_{13}
E_{11}, GPa	109	−3.9	−5.3	−192	287	−115	319	−209	−136
$E_{22,33}$, GPa	102	2.9	10.6	−111	325	−278	−17.8	−18.7	27
$G_{12,13}$, GPa	10.7	−0.1	0.25	−2.7	13	−10	−3.9	−0.1	4.1
G_{23}, GPa	2.5	−0.1	−0.06	−4.4	8	−3.4	6.4	−5	−2.5
$\nu_{12,13}$	0.011	−0.005	−0.009	−0.032	−0.038	0	−0.027	0.464	0
ν_{23}	0.017	−0.049	−0.017	−0.07	0.4	0	0.09	−0.18	0

It should be noted that the polynomial coefficients for Poisson's ratio can be reduced up to c_{00} because the influence of the parameters vector is insignificant. So, $\nu_{12,13} \approx 0.011$ and $\nu_{23} \approx 0.017$.

2.4. Proposed Algorithm

After the principal stress and directions are found, the orthotropic directions can be oriented according to the principal directions. The semi-major axis is directed to the 1st principal stress direction. The porosity is determined by von Mises stress and value $[\sigma]_{\text{inf}}$. The $[\sigma]_{\text{inf}}$ is the infimum of the stress value and determines the value of the underload. So, porosity can be restored by the equation:

$$\lambda\left(\vec{x}\right) = \begin{cases} 1 - \frac{[\sigma]_{\text{inf}} - \sigma_{V.M.}\left(\vec{x}\right)}{[\sigma]_{\text{inf}}}, \sigma_{V.M.}\left(\vec{x}\right) < [\sigma]_{\text{inf}} \\ 1, \sigma_{V.M.}\left(\vec{x}\right) \geq [\sigma]_{\text{inf}} \end{cases} \tag{14}$$

To determine the ellipticity coefficient, the 1st and the 3rd principal stresses were used:

$$\beta\left(\vec{x}\right) = \frac{\min\left(\left|\sigma_1\left(\vec{x}\right)\right|, \left|\sigma_3\left(\vec{x}\right)\right|\right)}{\max\left(\left|\sigma_1\left(\vec{x}\right)\right|, \left|\sigma_3\left(\vec{x}\right)\right|\right)} \tag{15}$$

Then, the stiffness constants can be calculated by porosity and the ellipticity coefficient and the stress-state problem can be solved. So, the algorithm can be described:

Algorithm of structural design

1. Load a *mesh* and apply *boundary conditions*.
2. Highlight *elements* from the *constant region* (8)
3. Set initial parameters vector
4. Solve the stress-state problem (1)–(6)
5. **for** each *element* not from *constant region*
6. Calculate the principal stress and directions
7. Calculate the parameters vector (14), (15)
8. Calculate stiffness tensor (13)
9. Orient element coordinate system according to the principal directions.
10. **end for**
11. **if** not *stop* **goto** 4
12. Restore geometry by parameters vector.

2.5. Model Task

A rectangular beam of 140 mm × 28 mm × 14 mm was used for the algorithm implementation. Eight-node hexahedral finite elements were used for the calculations. The kinematic loading of 1 mm was used in the numerical simulation. The length of the kinematic loading region was 20 mm. In Figure 2, the loading scheme is presented; the V_{con} region is marked by a green color. The end faces of the beam were fixed.

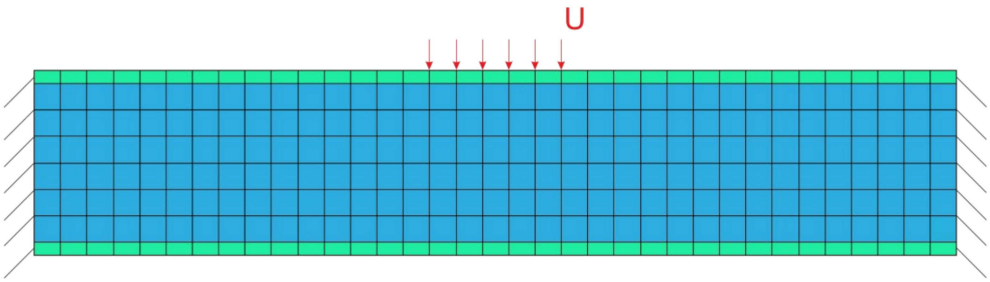

Figure 2. Loading scheme; U is applied displacements; the green region is V_{con} region.

The mechanical properties of acrylonitrile butadiene styrene were used for further production by additive manufacturing. So, Young's modulus was equal to 200 GPa, the shear modulus was equal to 71.5 GPa, and the Poisson ratio was 0.4. For $[\sigma]_{\text{inf}}$, 10% of maximum von Mises stress in the construction was used. The stop condition was as follows:

$$\max(|\lambda_i - \lambda_{i-1}|, |\beta_i - \beta_{i-1}|) < \varepsilon \tag{16}$$

where ε was equal to 10^{-3}.

2.6. Experiments

After restoring the geometry, the beam was produced by additive manufacturing technology. Acrylonitrile butadiene styrene was used for the manufacturing. Both the solid and the structural design samples were produced. For every two types of samples, longitudinal and transverse directions of printing were used. Computed tomography (CT) (Vatech PaX-I 3D, Kazan, Russia) was used to estimate the structure. After that, three-point

bending was carried out and stress-strain curves were obtained for all samples. For the stress-strain curves, the ultimate force and slope were analyzed.

3. Results and Discussion

The stress-strain state for the initial (solid) and the structurally designed beam were compared. The maximum stress did not change significantly, but the distribution of stress inside the product decreased (see Figure 3). The algorithm showed fast convergence; it was about 38 iterations. The maximum stress was localized in the zones of kinematic constraints for the initial geometry. In addition, for the structurally designed beam the maximum stress was localized in the zones of kinematic boundary conditions (see red regions in Figure 3). On the other hand, zones of stress reduction appeared for the structurally designed beam (see blue regions in Figure 3).

The distribution of the received porosity and ellipticity coefficients is shown in Figure 4. The zones of high porosity are localized where the von Misses stress was minimal (red zones in Figure 4a). In the same zones, the pore's ellipticity coefficient is close to 1 (red zones in Figure 4a), which means that in this region the pore is almost spherical.

The 3D geometry was restored for the following manufacturing (see Figure 5a). The initial and structurally designed samples were manufactured in two ways: longitudinal and transversal printing. After the manufacturing, the samples were scanned by CT (see Figure 5b,c). The deviations of pore geometry in the manufactured samples were noted. They were caused by the cooldown speed of the printing material drop. However, the distribution of the porosity was close enough to the design (deviations about 5%).

In the three-point bending experiments for the initial geometry, which was longitudinally printed, the maximum force was 1675 N, and the maximum displacement was 3.35 mm. For the structurally designed geometry, which was longitudinally printed, the maximum force was 1825 N, and the maximum displacement was 3.56 mm. A crack appeared in the middle, in the longitudinal direction between the kinematics constraints and the applied force (see Figure 6a). In the three-point bending experiments for the initial geometry, which was transversally printed, the maximum force was 7196 N, and the maximum displacement was 10.73 mm. For the structurally designed geometry, which was transversally printed, the maximum force was 6271 N, and the maximum displacement was 4.76 mm. A crack appeared under the applied force. The stress-strain curves for all the cases are shown in Figure 6b,c. The ultimate force deviation for the initial and structurally designed cases was about 10%, and it could be decreased by improving the manufacturing of the samples. A significant difference was noted for the displacements in the case of the transversal printing. The structurally designed sample became more rigid (4.76 mm vs. 10.73 mm).

Comparing the slope (for the longitudinal printing), a 25% increase was noted for the structurally designed sample (1184 N/mm and 1491 N/mm, respectively). The slope in the case of the transversal printing decreased by 20% for the structurally designed sample (710 N/mm and 894 N/mm, respectively).

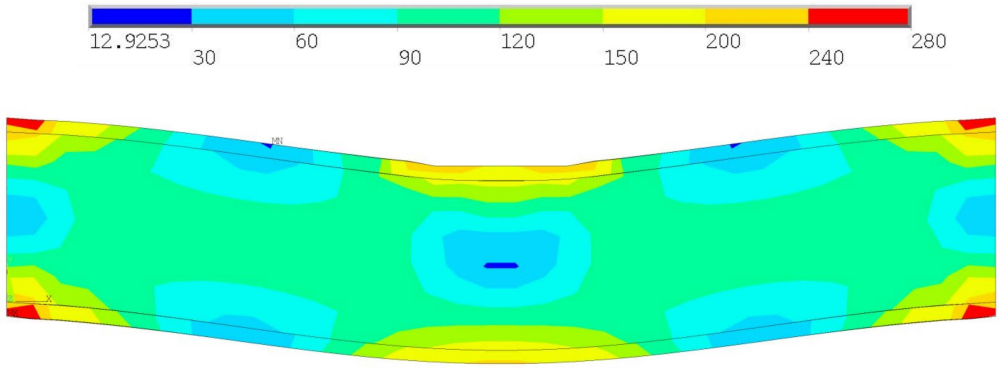

(**a**)

(**b**)

Figure 3. Von Mises stress distribution for initial (**a**) and structurally designed (**b**) beam.

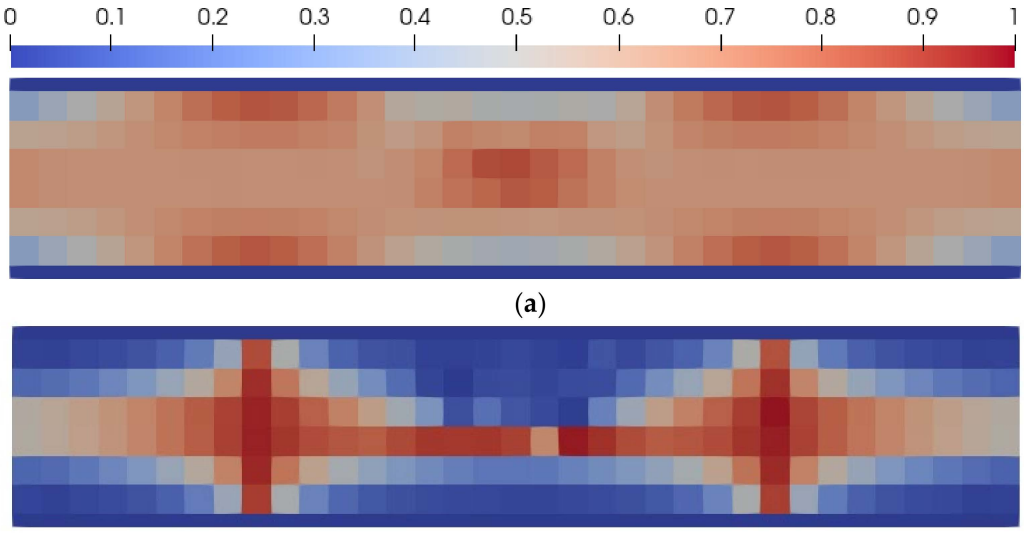

(**a**)

(**b**)

Figure 4. Distribution of porosity(**a**) and ellipticity coefficient (**b**).

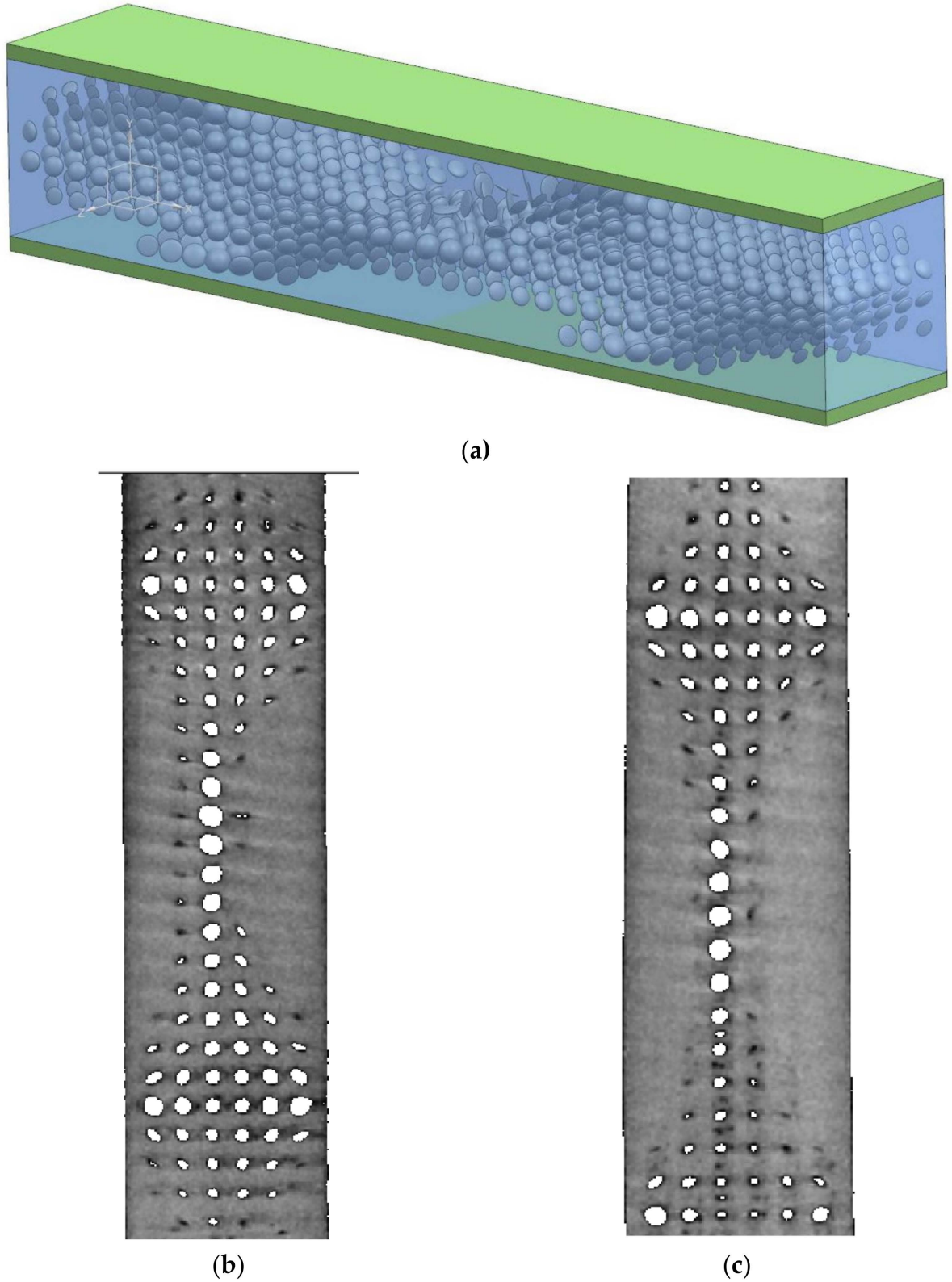

Figure 5. Restored 3D geometry (**a**), CT scans for longitudinal printing (**b**), and transversal printing (**c**).

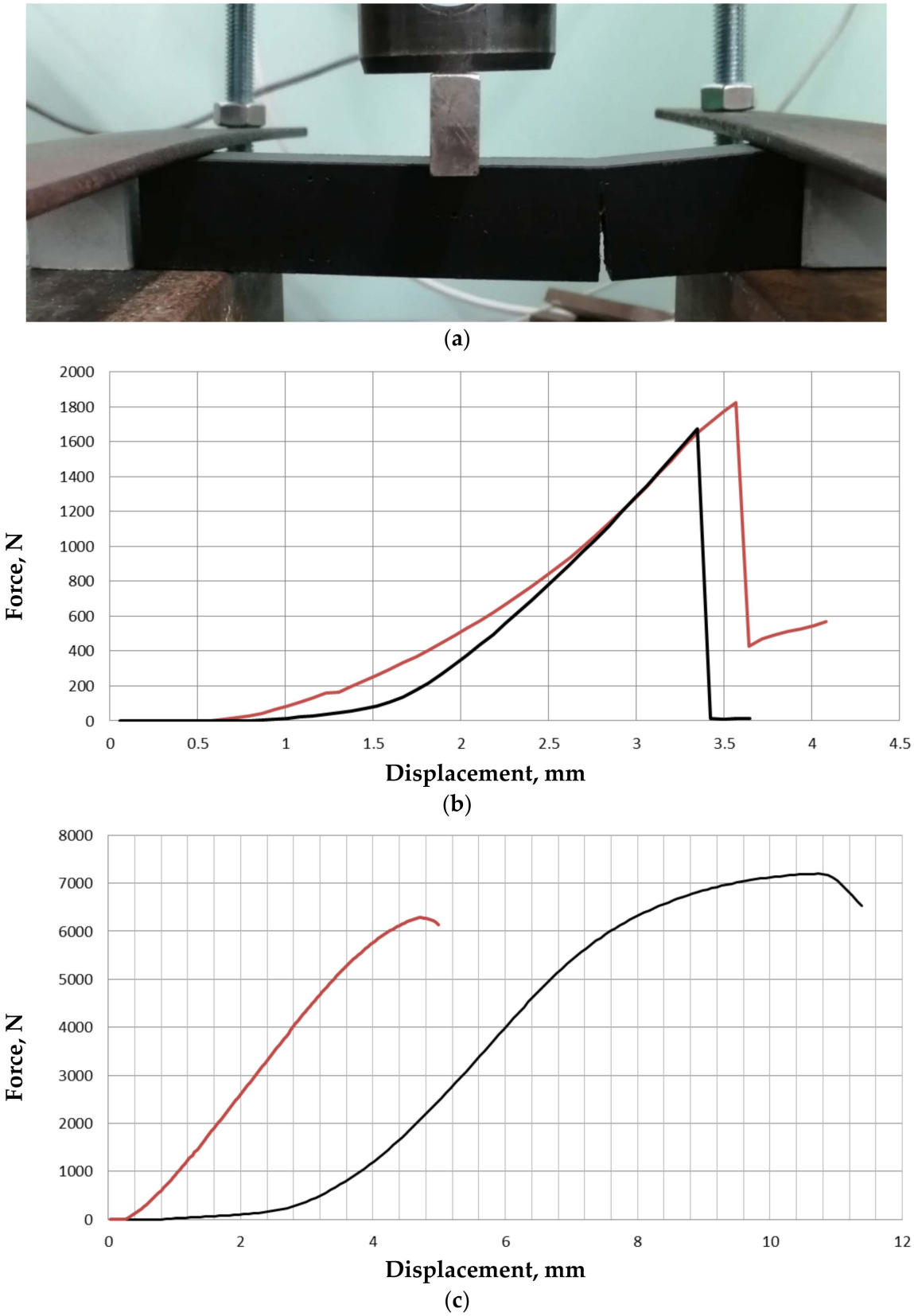

Figure 6. Three-point bending scheme (**a**), a stress-strain curve for longitudinal printing (**b**), and transversal printing (**c**); black lines—initial geometry, red lines—structurally designed geometry.

4. Conclusions

The algorithm for the structural design of the geometry was proposed. In the framework of the study, a porous cube was chosen for the basic cell. The following assumptions were used: calculation was carried out in an elastic zone; the material is isotropic; and anisotropy appears by the porosity of the basic cell. The iterative algorithm for the structural design was presented. The samples were designed, and the verification of the structural simulations was carried out. The comparison of the maximum von Mises stress for all the samples did not show a significant difference. However, for the structurally designed beam, zones of stress reduction appeared.

The manufacturing was provided using additive technologies. The samples were printed using different directions, and three-point bending tests were performed. Stress-strain curves were obtained for all the samples. In the case of the longitudinal direction printing, the ultimate force of the structurally designed sample was about 10% higher. In the case of the transversal direction printing, the rigidness of the structurally designed sample was almost 40% higher. The analysis of the stress-strain curves for all the samples shows the significant influence of the printing directions on the mechanical properties and demonstrated the need for post-processing.

Author Contributions: Methodology and software, P.B., N.K. and O.S.; manufacturing, R.K.; writing—review and editing, O.S.; conceptualization, O.S.; methodology, O.S. and P.B.; software, P.B. and N.K.; validation, O.S. and P.B.; formal analysis, P.B. and N.K.; investigation, P.B.; resources, R.K.; data curation, O.S.; writing—original draft preparation, P.B. and O.S.; writing—review and editing, O.S.; visualization, O.S. and P.B.; supervision, O.S.; project administration, O.S.; funding acquisition, O.S. and R.K. All authors have read and agreed to the published version of the manuscript.

Funding: This research was funded by RFBR, grant number 18-41-160025 p_a.

Institutional Review Board Statement: Not applicable.

Informed Consent Statement: Not applicable.

Data Availability Statement: Data available on request.

Acknowledgments: Special thanks to Independent X-ray diagnostic centers Picasso.

Conflicts of Interest: The authors declare no conflict of interest. The funders had no role in the design of the study; in the collection, analyses, or interpretation of data; in the writing of the manuscript; or in the decision to publish the results.

References

1. Ahmadi, S.; Campoli, G.; Yavari, S.A.; Sajadi, B.; Wauthle, R.; Schrooten, J.; Weinans, H.; Zadpoor, A.A. Mechanical behavior of regular open-cell porous biomaterials made of diamond lattice unit cells. *J. Mech. Behav. Biomed. Mater.* **2014**, *34*, 106–115. [CrossRef]
2. AlKhader, M.; Vural, M. Mechanical response of cellular solids: Role of cellular topology and microstructural irregularity. *Int. J. Eng. Sci.* **2008**, *46*, 1035–1051. [CrossRef]
3. Do, A.-V.; Khorsand, B.; Geary, S.M.; Salem, A.K. 3D Printing of Scaffolds for Tissue Regeneration Applications. *Adv. Health Mater.* **2015**, *4*, 1742–1762. [CrossRef] [PubMed]
4. Goda, I.; Ganghoffer, J.-F. 3D plastic collapse and brittle fracture surface models of trabecular bone from asymptotic homogenization method. *Int. J. Eng. Sci.* **2015**, *87*, 58–82. [CrossRef]
5. Li, P.; Wang, Z.; Petrinic, N.; Siviour, C.R. Deformation behaviour of stainless steel microlattice structures by selective laser melting. *Mater. Sci. Eng. A.* **2014**, *614*, 116–121. [CrossRef]
6. Limmahakhun, S.; Oloyede, A.; Sitthiseripratip, K.; Xiao, Y.; Yan, C. 3D-printed cellular structures for bone biomimetic implants. *Addit. Manuf.* **2017**, *15*, 93–101. [CrossRef]
7. Limmahakhun, S.; Oloyede, A.; Sitthiseripratip, K.; Xiao, Y.; Yan, C. Stiffness and strength tailoring of cobalt chromium graded cellular structures for stress-shielding reduction. *Mater. Des.* **2017**, *114*, 633–641. [CrossRef]
8. Bari, K.; Arjunan, A. Extra low interstitial titanium based fully porous morphological bone scaffolds manufactured using selective laser melting. *J. Mech. Behav. Biomed. Mater.* **2019**, *95*, 1–12. [CrossRef]
9. Concli, F.; Gilioli, A. Numerical and experimental assessment of the mechanical properties of 3D printed 18-Ni300 steel trabecular structures produced by Selective Laser Melting—A lean design approach. *Virtual Phys. Prototyp.* **2019**, *14*, 267–276. [CrossRef]

10. Mukhopadhyay, T.; Adhikari, S. Effective in-plane elastic moduli of quasi-random spatially irregular hexagonal lattices. *Int. J. Eng. Sci.* **2017**, *119*, 142–179. [CrossRef]
11. Bolshakov, P.; Raginov, I.; Egorov, V.; Kashapova, R.; Kashapov, R.; Baltina, T.; Sachenkov, O. Design and Optimization Lattice Endoprosthesis for Long Bones: Manufacturing and Clinical Experiment. *Materials* **2020**, *13*, 1185. [CrossRef] [PubMed]
12. Cowin, S.C.; Sadegh, A.M.; Luo, G.M. An evolutionary wolff's law for trabecular architecture. *J. Biomech. Eng.* **1992**, *114*, 129–136. [CrossRef] [PubMed]
13. Maquer, G.; Musy, S.N.; Wandel, J.; Gross, T.; Zysset, P.K. Bone volume fraction and fabric anisotropy are better determinants of trabecular bone stiffness than other morphological variables. *J. Bone Miner. Res.* **2015**, *30*, 1000–1008. [CrossRef]
14. Gross, T.; Pahr, D.H.; Zysset, P.K. Morphology-elasticity relationships using decreasing fabric information of human trabecular bone from three major anatomical locations. *Biomech. Modeling Mechanobiol.* **2013**, *12*, 793–800. [CrossRef] [PubMed]
15. Pahr, D.H.; Zysset, P.K. A comparison of enhanced continuum FE with micro FE models of human vertebral bodies. *J. Biomech.* **2009**, *42*, 455–462. [CrossRef] [PubMed]
16. Kharin, N.V.; Vorobyev, O.V.; Berezhnoi, D.V.; Sachenkov, O.A. Construction of a representative model based on computed tomography. *PNRPU Mech. Bull.* **2018**, *3*, 95–102. [CrossRef]
17. Maslov, L.B. Mathematical Model of Bone Regeneration in a Porous Implant. *Mech. Compos. Mater.* **2017**, *53*, 399–414. [CrossRef]
18. Maslov, L. Mathematical modelling of the mechanical properties of callus restoration. *J. Appl. Math. Mech.* **2015**, *79*, 195–206. [CrossRef]
19. Kirpichev, I.V.; Korovin, D.I.; Maslov, L.B.; Tomin, N.G. Mathematical model of cell transformations at bone tissue regeneration under alterating biochemical medium with possible mechanoregulation. *Russ. J. Biomech.* **2016**, *20*, 187–201.
20. Maslov, L.; Surkova, P.; Maslova, I.; Solovev, D.; Zhmaylo, M.; Kovalenko, A.; Bilyk, S. Finite-element study of the customized implant for revision hip replacement. *Vibroeng. PROCEDIA* **2019**, *26*, 40–45. [CrossRef]
21. Tikhilov, R.M.; Konev, V.A.; Shubnyakov, I.I.; Denisov, A.O.; Mikhailova, P.M.; Bilyk, S.S.; Kovalenko, A.N.; Starchik, D.A. Additive technologies for complete recovery of joint function in revision endoprosthesis surgery (experimental trial). *Khirurgiya. Zhurnal Im. N.I. Pirogova* **2019**, *5*, 52–56. [CrossRef]
22. Hettich, G.; Schierjott, R.A.; Epple, M.; Gbureck, U.; Heinemann, S.; Jovein, M.-; Grupp, T.M.; Mozaffari-Jovein, H. Calcium Phosphate Bone Graft Substitutes with High Mechanical Load Capacity and High Degree of Interconnecting Porosity. *Materials* **2019**, *12*, 3471. [CrossRef] [PubMed]
23. Scheele, C.B.; Pietschmann, M.; Schröder, C.; Lazic, I.; Grupp, T.M.; Müller, P.E. Influence of bone density on morphologic cement penetration in minimally invasive tibial unicompartmental knee arthroplasty: An in vitro cadaver study. *J. Orthop. Surg. Res.* **2019**, *14*, 331–339. [CrossRef] [PubMed]
24. Kaplun, B.W.; Zhou, R.; Jones, K.W.; Dunn, M.L.; Yakacki, C.M. Influence of orientation on mechanical properties for high-performance fused filament fabricated ultem 9085 and electro-statically dissipative polyetherketoneketone. *Addit. Manuf.* **2020**, *36*, 101527.
25. Tilton, M.; Lewis, G.S.; Hast, M.W.; Fox, E.; Manogharan, G. Additively manufactured patient-specific prosthesis for tumor reconstruction: Design, process, and properties. *PLoS ONE* **2021**, *16*, e0253786. [CrossRef]
26. Kuchumov, A.G.; Selyaninov, A. Application of computational fluid dynamics in biofluids simulation to solve actual surgery tasks. *Adv. Intell. Syst. Comput.* **2020**, *1018*, 576–580. [CrossRef]
27. Kamenskih, A.; Astashina, N.B.; Lesnikova, Y.; Sergeeva, E.; Kuchumov, A.G. Numerrical and experimental study of the functional loads distribution in the dental system to evaluate the new design of the sports dental splint. *Ser. Biomech.* **2018**, *32*, 3–15.
28. Traugutt, N.A.; Mistry, D.; Luo, C.; Yu, K.; Ge, Q.; Yakacki, C.M. Liquid-Crystal-Elastomer-Based Dissipative Structures by Digital Light Processing 3D Printing. *Adv. Mater.* **2020**, *32*, 2000797. [CrossRef]
29. Shaha, R.K.; Merkel, D.R.; Anderson, M.P.; Devereaux, E.J.; Patel, R.R.; Torbati, A.H.; Willett, N.; Yakacki, C.M.; Frick, C.P. Biocompatible liquid-crystal elastomers mimic the intervertebral disc. *J. Mech. Behav. Biomed. Mater.* **2020**, *107*, 103757. [CrossRef]
30. Mori, T.; Cukelj, R.; Prévôt, M.E.; Ustunel, S.; Story, A.; Gao, Y.; Diabre, K.; McDonough, J.A.; Freeman, E.J.; Hegmann, E.; et al. 3D Porous Liquid Crystal Elastomer Foams Supporting Long-term Neuronal Cultures. *Macromol. Rapid Commun.* **2020**, *41*, 1900585. [CrossRef] [PubMed]
31. Kharin, N.; Vorob'Yev, O.; Bol'Shakov, P.; Sachenkov, O. Determination of the orthotropic parameters of a representative sample by computed tomography. *J. Phys. Conf. Ser.* **2019**, *1158*, 032012. [CrossRef]
32. Vahterova, Y.A.; Fedotenkov, G.V. The inverse problem of recovering an unsteady linear load for an elastic rod of finite length. *J. Appl. Eng. Sci.* **2020**, *18*, 687–692. [CrossRef]
33. Fedotenkov, G.V.; Makarevskiiy, D.I.; Vahterova, Y.V.; Thang, T.Q. The inverse non-stationary problem of identification of defects in an elastic rod. *INCAS Bull.* **2021**, *13*, 57–66. [CrossRef]
34. Kayumov, R.A.; Muhamedova, I.Z.; Tazyukov, B.F.; Shakirzjanov, F.R. Parameter determination of hereditary models of deformation of composite materials based on identification method. *J. Phys. Conf. Ser.* **2018**, *973*, 012006. [CrossRef]
35. Kayumov, R.A. Structure of nonlinear elastic relationships for the highly anisotropic layer of a nonthin shell. *Mech. Compos. Mater.* **1999**, *35*, 409–418. [CrossRef]
36. Kharin, N.V.; Gerasimov, O.V.; Bolshakov, P.V.; Khabibullin, A.A.; Fedyanin, A.O.; Baltin, M.E.; Baltina, T.V.; Sachenkov, O.A. Technique for determining the orthotropic properties of the bone organ according to computer tomography. *Russ. J. Biomech.* **2019**, *23*, 395–402. [CrossRef]